Supplement of Atmos. Chem. Phys., 22, 9721–9745, 2022
https://doi.org/10.5194/acp-22-9721-2022-supplement

Supplement of

Circum-Antarctic abundance and properties of CCN and INPs

Christian Tatzelt et al.

Correspondence to: Silvia Henning (silvia.henning@tropos.de) and Julia Schmale (julia.schmale@epfl.ch)

Contents

Text S1 describes the analysis of the 10 d backward-trajectories with regards to air-mass origin. Figure S1 is an example for the applied mode-fitting procedure to the particle number size distributions.

Figure S2 is an overview on the spatial distribution of N_{CCN}, presented as daily mean values. Table S1 is an overview on the N_{total}, N_{CCN}, D_{crit}, and κ values encountered during ACE. Figure S3 shows a sensitivity analysis of derived κ values towards the applied methods and criteria.

Figure S4 is an overview on the spatial distribution of the N_{INP} values from the LV filters. Figure S5 is an overview on the results of the INP analysis of the HV filters. Figure S6 shows the results of the analysis of the 10 d backward-trajectories regarding the air-mass origin for the LV filters. Figure S7 shows the dependence of Antarctic and non-Antarctic terrestrial signal in air-mass origin on the N_{INP} for the LV filters. Figure S8 shows the temperature-dependence of N_{INP}, n_{s}, and n_{v} for the LV filters. Table S2 is an overview on the average N_{INP} encountered during the cruise. Table S3 is an overview on the averaged N_{INP} of the field blank filters (FBF). Table S4 is the overview on the average N_{INP} of the HV filters.

Table S5 is the overview on the mass concentration values (M) for PM_{10} mass, sodium, and MSA.

S1: Analysis of the air-mass origin for LV sampling

Backward-trajectories for ACE are available in Thurnherr et al. (2020). They used the "LAGRNgian analysis TOol" (LAGRATO) described in Sprenger and Wernli (2015) with reanalysis data from the European Centre for Medium Range Weather Forecasts (ECMWF). These reanalyses are produced by the ECMWF Integrated Forecasting System (IFS), an atmospheric model and data assimilation system. These trajectories were used to analyse the air-mass origin in terms of geographical and surface information. At an hourly resolution, trajectories are available for 56 pressure levels (between the surface and 500 hPa above sea level) above the RV's position. To achieve more robust statistics, for each hour all trajectories ending within the planetary boundary layer (PBL) above the RV's position are averaged into a cluster by calculating median values of latitude, longitude, pressure level, boundary layer pressure level, total precipitation, land fraction and sea ice fraction. The initial step in this analysis is the application of a rain filter on each cluster. Here, it is assumed that aerosol particles are removed from the atmosphere by scavenging and wet deposition during precipitation events. Similar to Herenz et al. (2019), a total precipitation (R_{total}) threshold of $0.1\,\mathrm{mm\,h^{-1}}$ between hourly time steps is used. Since the air parcel that is described by the trajectory has it's parameters calculated every three hours, the threshold in R_{total} is 0.3 mm between time steps. If $R_{\mathrm{total}}(t)$ exceeds this threshold, all time steps prior to t are excluded from the analysis. In the special case of a rain event occurring at the RV's position, the entire cluster is excluded from the analysis. As the second step of the analysis, for each cluster the air parcel's pressure level at each time step $p(t)$ is compared to the pressure level of the PBL ($p_{\mathrm{PBL}}(t)$). A time step is classified as free tropospheric if $p(t) < p_{\mathrm{PBL}}(t)$ and it is assumed that the air parcel did not collect any aerosol signal from the surface. In the case of $p(t) > p_{\mathrm{PBL}}(t)$, the surfaces type below the air parcel is categorised. Here, the IFS's land-sea mask is used for initial classification of the surface signal type. If the land-sea mask indicates that the entire surface in the grid box is land, the surface signal is classified as "land". Correspondingly, if the entire grid box is over a body of water, the surface type is classified as "sea". If the land-sea mask indicates neither "land" nor "sea", the surface type is classified as "coast". If the surface below the air parcel is identified as being a body of water, the IFS's sea ice fraction is used to discriminate if it is open ocean or covered by sea ice. A commonly used sea ice fraction threshold of $< 15\,\%$ is applied here to classify as "open ocean" (following Cavalieri et al., 1991). A sea ice fraction threshold of $> 80\,\%$ is used to classify "sea ice". Any sea ice fraction between "sea ice" and "open ocean" is classified as "marginal ice zone" (MIZ). If the surface below the air parcel is classified as "land" or "coast", geographical polygons from the air-mass source appointment tool "TRACE" (Radenz et al., 2021) are used to determine from which land-mass the surface signal stems. Three polygons from TRACE have been used, roughly outlining Africa, Australia, and South

America. If the geo-location of the air parcel is outside of the three polygons, it is classified as "unidentified". The final step of the analysis is the averaging of PBL signals from all clusters within each LV filter's 8 h sampling period. The total number of trajectories that are averaged in clusters and considered per LV filter is between 1 and 28, with a mean of roughly 15.

Results of each step of this analysis are illustrated in Fig. S6. The number of considered trajectories and how much time steps are cut due to the application of the precipitation filter are illustrated in Fig. S6a. The ratio between free tropospheric and PBL signal is given in Fig. S6b. The contribution of each surface type below the air parcel for the PBL signals is indicated in Fig. S6c. Information on the geographical location below the air parcel for each PBL signal is given in Fig. S6d.

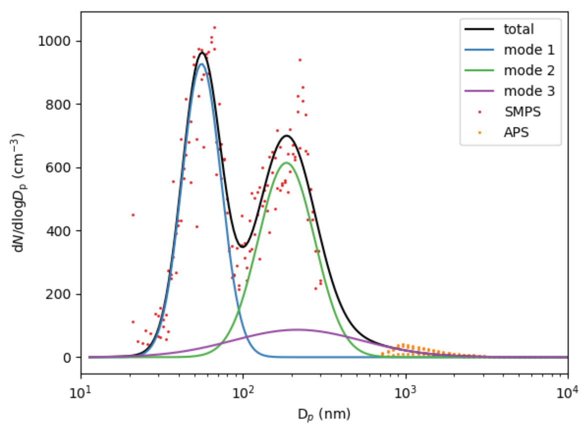

Figure S1. An example for the results of the mode-fitting approach applied to the output of the Scanning Mobility Particle Sizer (SMPS) and Aerodynamic Particle Sizer (APS) instruments. Particle number size distributions (PNSDs) from the SMPS (red) and APS instruments (orange) are given as dots. The three fitted log-normal distributions (Aitken mode, blue; accumulation mode, green; sea spray mode, purple) and the sum of the three modes (total PNSD, black) are given as lines.

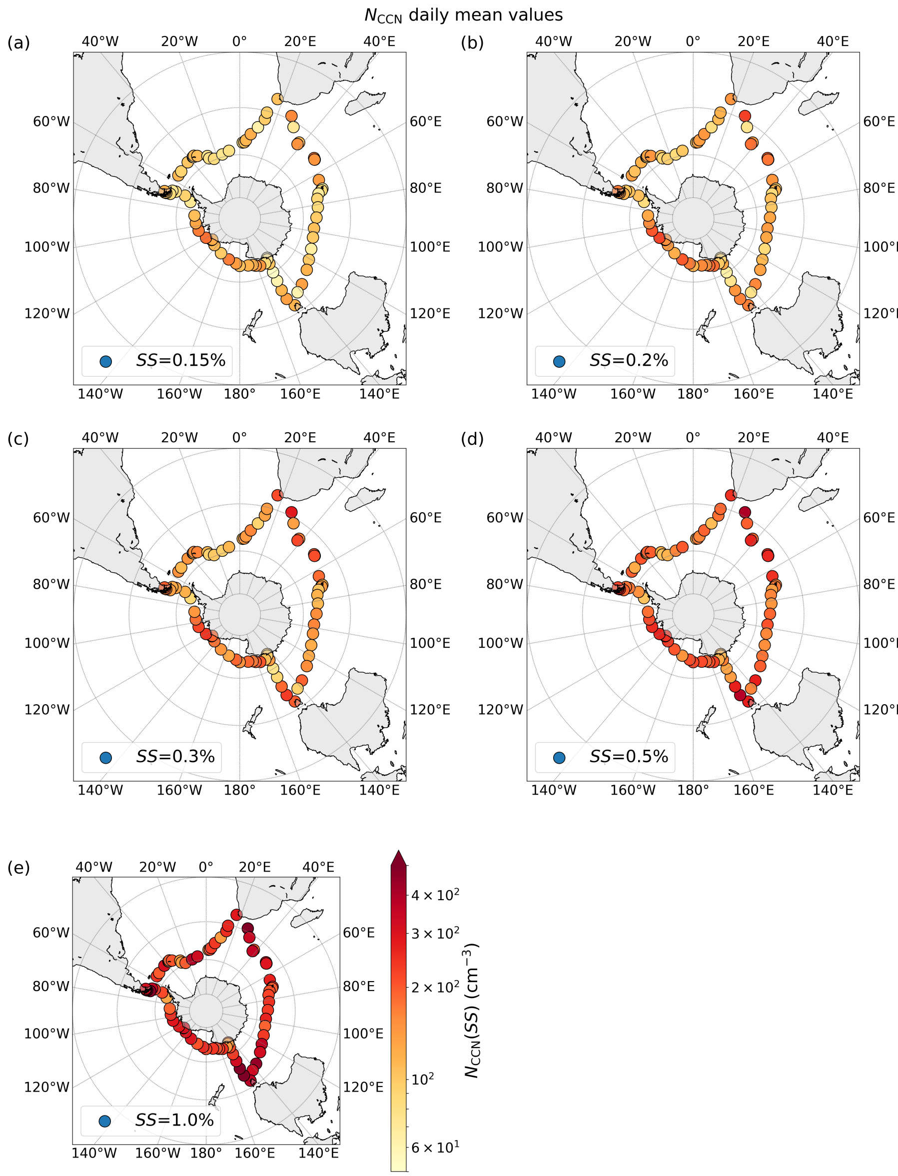

Figure S2. Average daily values of CCN number concentration (N_{CCN}) at a supersaturation (SS) of (a) 0.15, (b) 0.2, (c) 0.3, (d) 0.5, and (e) 1 % throughout the cruise, given at the midpoint of the respective cruise track of that day.

Table S1. Overview of the CCN number concentration (N_{CCN}) and critical dry diameter (D_{crit}) values at a given level of supersaturation (SS) throughout and for parts of the cruise, given as geometric mean value (and a factor of respective one geometric standard deviation). Additionally, the averages of the total particle concentration (N_{total}) and the aerosol particle hygroscopicity parameter (κ) at given SS presented as median values and respective inter-quartile range.

	Legs 1–3	Leg 1	Leg 2	Leg 3
N_{total} (cm^{-3})	305.04 (225.77, 451.84)	389.75 (272.06, 539.29)	277.00 (211.34, 382.17)	318.76 (235.02, 442.93)
$N_{\mathrm{CCN}}(SS)$ (cm^{-3})				
$SS = 0.15\,\%$	88.64 (53.28, 147.48)	90.49 (52.04, 157.33)	94.20 (59.19, 149.92)	78.61 (47.29, 130.69)
$SS = 0.2\,\%$	111.79 (67.98, 183.82)	113.56 (67.28, 191.67)	119.48 (76.03, 187.76)	98.63 (58.85, 165.29)
$SS = 0.3\,\%$	132.52 (79.41, 221.16)	133.83 (80.84, 221.54)	143.39 (88.97, 231.11)	115.50 (66.95, 199.27)
$SS = 0.5\,\%$	171.69 (101.49, 290.47)	172.18 (106.83, 277.51)	185.44 (111.84, 307.47)	150.71 (84.43, 269.05)
$SS = 1\,\%$	247.98 (145.28, 423.28)	241.12 (157.20, 369.82)	257.79 (146.73, 452.92)	239.56 (133.96, 428.39)
$D_{\mathrm{crit}}(SS)$ (nm)				
$SS = 0.15\,\%$	109.40 (100.29, 119.34)	112.56 (101.94, 124.29)	108.61 (99.91, 118.07)	110.05 (100.98, 119.94)
$SS = 0.2\,\%$	84.07 (72.77, 97.12)	89.86 (75.98, 106.28)	81.78 (71.46, 93.59)	86.52 (75.97, 98.54)
$SS = 0.3\,\%$	66.23 (56.37, 77.83)	72.77 (60.36, 87.72)	64.15 (55.43, 74.24)	66.73 (57.51, 77.42)
$SS = 0.5\,\%$	47.04 (39.98, 55.34)	52.23 (42.01, 63.42)	45.58 (39.42, 52.69)	47.18 (40.84, 54.52)
$SS = 1\,\%$	30.22 (25.73, 35.48)	32.90 (27.73, 39.04)	29.46 (25.20, 34.44)	30.22 (26.18, 34.88)
$\kappa(SS)$				
$SS = 0.15\,\%$	0.50 (0.40, 0.60)	0.42 (0.33, 0.53)	0.51 (0.42, 0.61)	0.48 (0.40, 0.59)
$SS = 0.2\,\%$	0.61 (0.44, 0.82)	0.43 (0.30, 0.66)	0.67 (0.50, 0.89)	0.54 (0.42, 0.72)
$SS = 0.3\,\%$	0.57 (0.39, 0.78)	0.36 (0.24, 0.60)	0.63 (0.46, 0.84)	0.55 (0.41, 0.73)
$SS = 0.5\,\%$	0.55 (0.39, 0.79)	0.34 (0.23, 0.58)	0.60 (0.45, 0.84)	0.54 (0.40, 0.74)
$SS = 1\,\%$	0.52 (0.38, 0.70)	0.39 (0.24, 0.54)	0.55 (0.42, 0.76)	0.52 (0.38, 0.68)

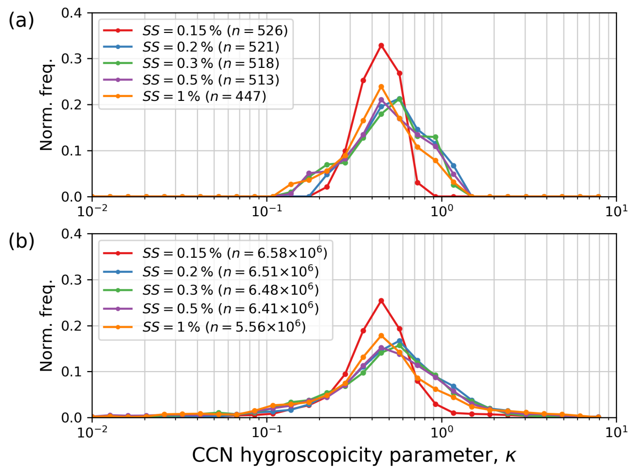

Figure S3. Normalized probability density function of hygroscopicity parameter (κ) for levels of supersaturation 0.15, 0.2, 0.3, 0.5, 1 % (SS, colour-coded) for Legs 1–3. Monte-Carlo simulations were performed to assess the measurement uncertainty for (b) and not performed for (a). In (b) κ values that resulted from D_{crit} outside of 10th to 90th percentile range (per SS) were excluded for (a) but not for (b). The number of data points are indicated (n) in the figure.

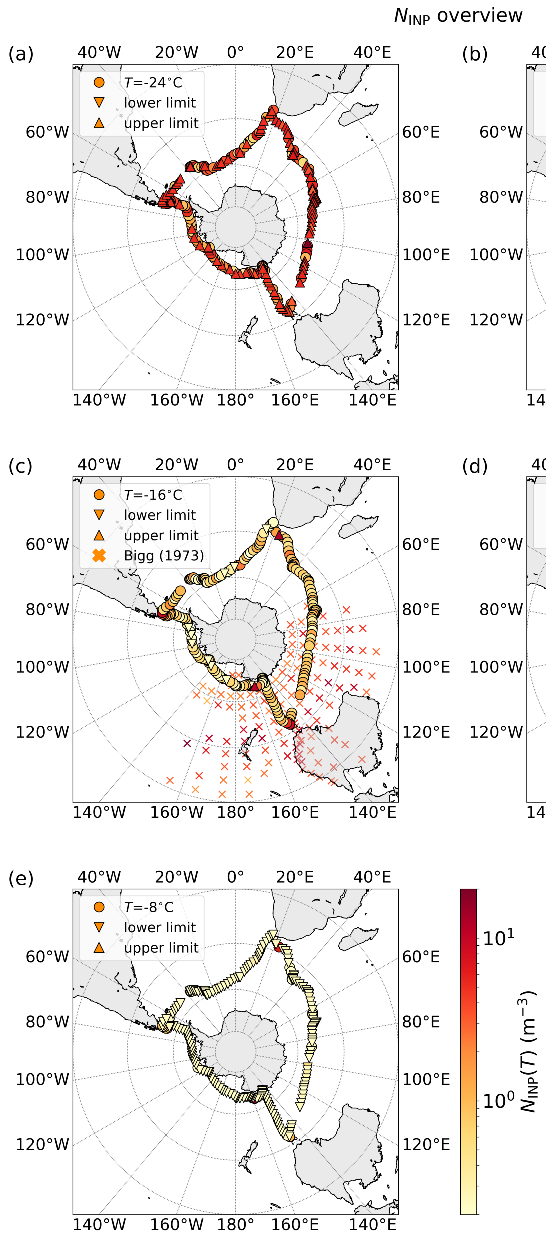

Figure S4. INP number concentration at (a) −24, (b) −20, (c) −16, (d) −12, and (e) −8°C for the LV filters sampled during ACE (circles). Filters at lower (upper) end of detectable range are indicated as downward (upward) triangles. The marker position indicates the midpoint between the RV's position of the the start and the end of the 8 h sampling period. Values of $N_{\mathrm{INP},-15}$ from Bigg (1973) are provided in (c) for comparison (crosses). A correction of the $N_{\mathrm{INP},-15}$ values from Bigg (1973) was applied, following the supporting information to McCluskey et al. (2018).

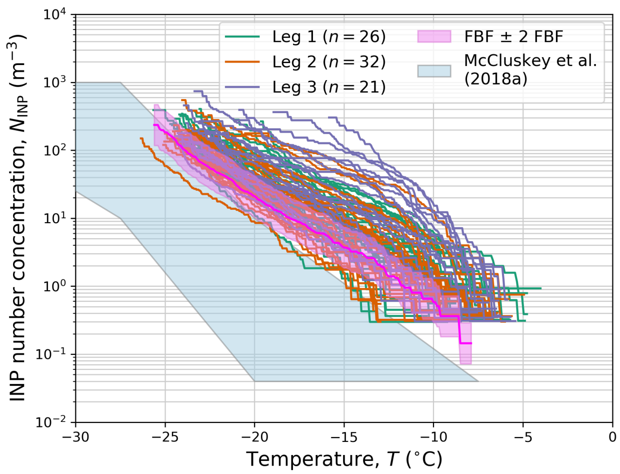

Figure S5. INP number concentration (N_{INP}) as function of temperature (T) for the HV filters sampled during ACE. Average spectra of field blank filters (FBF) ± a factor of two (pink line and area) and data range from McCluskey et al. (2018) (light blue envelope) are given for reference. The number of samples are indicated (n) in the figure.

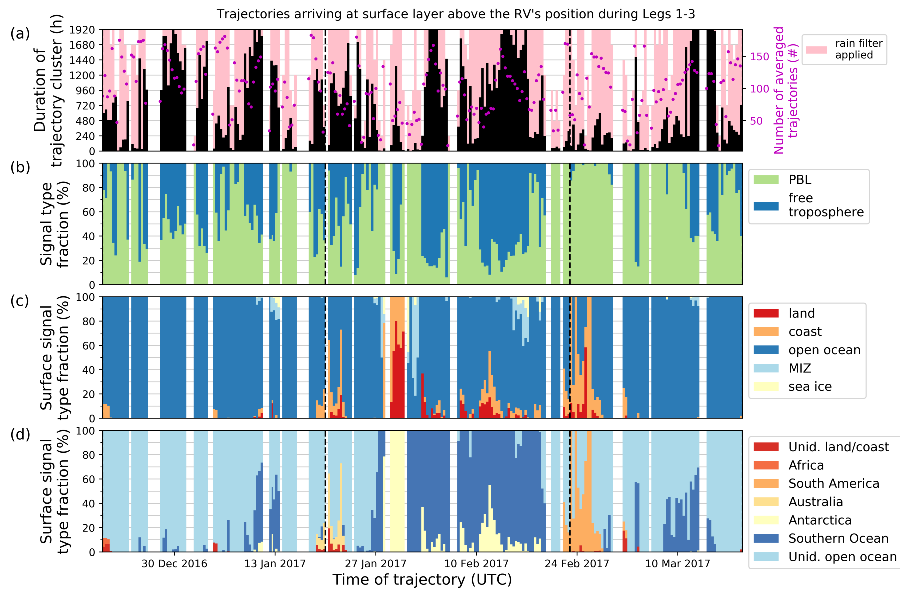

Figure S6. Results of the analysis of the 10 d backward-trajectories calculated for ACE regarding potential aerosol particle signals. Hourly-available trajectories ending within the PBL above the RV's position have been averaged into clusters and in (a) the total number of averaged trajectories per 8 h window is given (purple). In addition, the duration of each trajectory cluster is given with the part considered for the analysis (black) and the part omitted due to the applied rain filter indicated (pink). In (b) the normalized contribution of planetary boundary layer (PBL; green) and free tropospheric signal (blue) in the considered, average trajectories is given. In (c) the surface signal is specified as land (red), coast (orange), open ocean ($f_{\mathrm{SI}} \leq 15\,\%$; dark blue), marginal ice zone ($15\,\% < f_{\mathrm{SI}} \leq 80\,\%$; light blue), or sea ice ($f_{\mathrm{SI}} > 80\,\%$; yellow) resulting from the European Centre for Medium Range Weather Forecasts (ECMWF) analyses' additional information on the land and sea ice fraction (f_{SI}). Similarly, information on the geographical position is given in (d) using the polygons for Africa, South America, Australia and Antarctica in Radenz et al. (2021). The trajectories for ACE are available in Thurnherr et al. (2020).

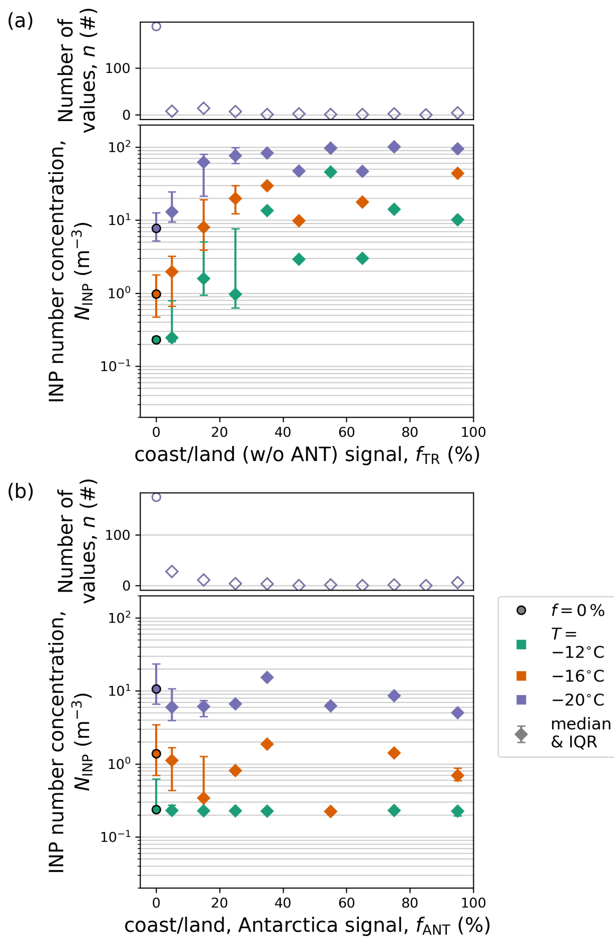

Figure S7. Median and respective inter-quartile range (IQR) of INP number concentration (N_{INP}) at a T of $-12°$C (green), $-16°$C (orange), and $-20°$C (purple) as function of (a) non-Antarctic terrestrial signal and (b) Antarctic terrestrial signal. In addition, the median value and respective IQR for N_{INP} in oceanic air-masses (circle) and number of considered values for the averaging (n) are included in the figure.

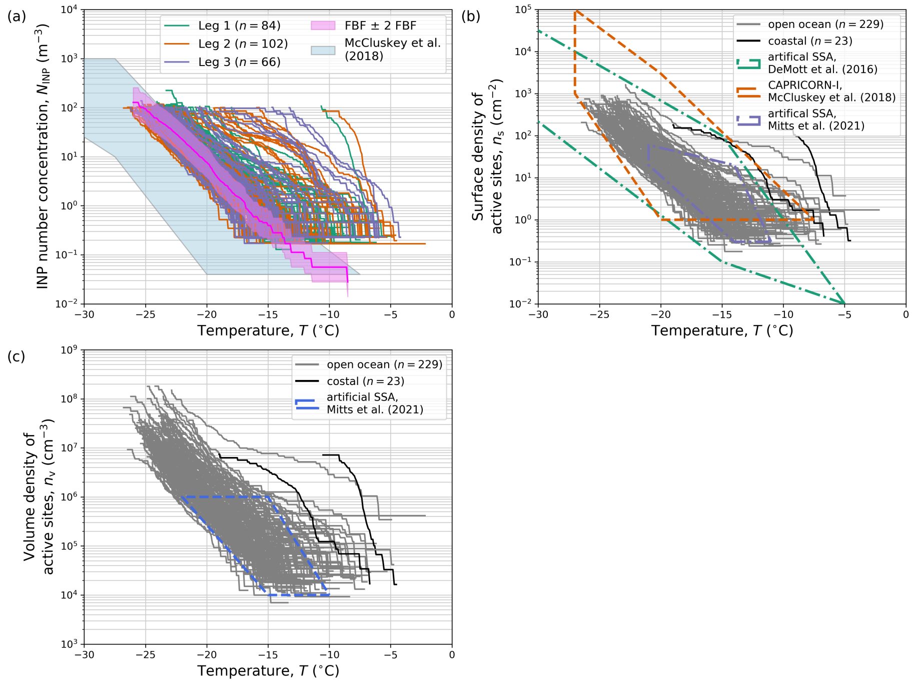

Figure S8. Temperature-dependence of (a) INP number concentration N_{INP}, (b) surface density of active sites n_{s}, and (c) volume density of active sites n_{v} for the LV filters sampled during ACE. Values of n_{s} (n_{v}) were calculated by normalising N_{INP} with the total particle surface area (total particle volume) derived from an averaged particle number size distribution per filter under the assumption of a population of only spherical particles. In (a) the data set is divided into Leg 1 (green), Leg 2 (orange), and Leg 3 (purple). In (b) and (c) the data set is divided into open ocean (gray) and coastal (black) based on the threshold in $N_{\mathrm{INP},-16}$ of $10\,\mathrm{m}^{-3}$ (see Fig. 8c). In (a) the measurement background from averaged spectra of field blank filters (FBFs) $\pm$ a factor of two (pink line and area) and the data range from McCluskey et al. (2018) is given for reference (light blue area). In (b) data ranges from DeMott et al. (2016) (green), McCluskey et al. (2018) (orange) and Mitts et al. (2021) (purple) are given for reference. The range of values (dashed) from Mitts et al. (2021) is given in (c) for reference. The number of samples (n) are indicated in the figure.

Table S2. Overview of the LV sampling INP number concentrations ($N_{\mathrm{INP,LV}}$) measured throughout the cruise, given as mean, median, and geometric mean values (including one geometric standard deviation). For this averaging only concentrations within the detectable range are considered and the number of samples, n, are indicated in the table. In the lower part, averages including concentrations at the upper/lower boundaries of sensitivity (see subsections 2.3 and 3.2) are given as $N^{\star}_{\mathrm{INP}}$.

	mean	median	$\mathrm{mean_{geo}}$ ($\mathrm{SD_{geo}}$)	n
$N_{\mathrm{INP,LV}}(T)$ ($\mathrm{m^{-3}}$)				
$T = -24$°C	66.95	64.78	61.45 (40.07, 94.25)	105
$T = -20$°C	13.87	8.57	9.43 (4.21, 21.15)	237
$T = -16$°C	4.41	1.18	1.44 (0.41, 5.10)	237
$T = -12$°C	2.66	0.42	0.72 (0.17, 2.99)	120
$T = -8$°C	1.67	0.46	0.58 (0.18, 1.84)	46
$N^{\star}_{\mathrm{INP,LV}}(T)$ ($\mathrm{m^{-3}}$)				
$T = -24$°C	85.22	97.65	80.39 (55.48, 116.48)	252
$T = -20$°C	18.75	8.84	10.82 (4.16, 28.15)	252
$T = -16$°C	6.11	1.17	1.46 (0.35, 5.97)	252
$T = -12$°C	2.15	0.23	0.41 (0.12, 1.43)	252
$T = -8$°C	0.49	0.23	0.27 (0.14, 0.50)	252

Table S3. Mean INP number concentration of field blank filters (FBFs) for LV sampling ($N_{\mathrm{INP,LV,FBF}}$) and HV sampling ($N_{\mathrm{INP,HV,FBF}}$) at selected temperatures (T).

	$N_{\mathrm{INP,LV,FBF}}(T)$ (m^{-3})	$N_{\mathrm{INP,HV,FBF}}(T)$ (m^{-3})
$T = -24°\mathrm{C}$	57.76	105.11
$T = -20°\mathrm{C}$	7.72	21.08
$T = -16°\mathrm{C}$	0.59	5.64
$T = -12°\mathrm{C}$	0.08	1.32
$T = -8°\mathrm{C}$	-	0.14

Table S4. Overview of the HV sampling INP number concentrations ($N_{\mathrm{INP,HV}}$) measured throughout the cruise, given as mean, median, and geometric mean values (including one geometric standard deviation). Averaging was performed with the inclusion of concentrations on the lower/upper boundaries of sensitivity and the number of samples (n) are indicated in the table. Differences in sampling strategy for HV compared to LV samples can be found in subsection 2.3.

	mean	median	$\mathrm{mean_{geo}}$ ($\mathrm{SD_{geo}}$)	n
$N_{\mathrm{INP,HV}}(T)$ ($\mathrm{m^{-3}}$)				
$T = -24$°C	206.08	176.07	185.52 (118.70, 289.94)	79
$T = -20$°C	70.28	40.63	48.52 (21.51, 109.45)	79
$T = -16$°C	25.03	12.81	13.39 (4.77, 37.60)	79
$T = -12$°C	6.82	3.10	3.17 (0.90, 11.15)	79
$T = -8$°C	0.94	0.54	0.69 (0.34, 1.43)	79

Table S5. Overview of PM_{10}, sodium and methanesulfonic acid (MSA) mass concentrations M throughout ACE and for parts of it, given as median (inter-quartile range) values.

M ($\mu g\,m^{-3}$)	Legs 1–3	Leg 1	Leg 2	Leg 3
PM_{10}	32.35 (26.05, 49.60)	42.40 (27.30, 52.60)	31.05 (23.48, 47.48)	33.30 (26.20, 50.70)
sodium	2.75 (1.81, 3.89)	3.55 (2.56, 4.92)	1.81 (0.97, 3.15)	2.75 (2.24, 4.10)
MSA	0.10 (0.07, 0.14)	0.11 (0.08, 0.18)	0.11 (0.07, 0.21)	0.09 (0.06, 0.10)

References

Bigg, E.: Ice nucleus concentrations in remote areas, J. Atmos. Sci., 30, 1153–1157, https://doi.org/10.1175/1520-0469(1973)030⟨1153:INCIRA⟩2.0.CO;2, 1973.

Cavalieri, D. J., Crawford, J. P., Drinkwater, M. R., Eppler, D. T., Farmer, L. D., Jentz, R. R., and Wackerman, C. C.: Aircraft active and passive microwave validation of sea ice concentration from the Defense Meteorological Satellite Program special sensor microwave imager, J. Geophys. Res.-Oc., 96, 21 989–22 008, https://doi.org/10.1029/91JC02335, 1991.

DeMott, P., Hill, T., McCluskey, C., Prather, K., Collins, D., Sullivan, R., Ruppel, M., Mason, R., Irish, V., Lee, T., Hwang, C., Rhee, T., Snider, J., McMeeking, G., Dhaniyala, S., Lewis, E., Wentzell, J., Abbatt, J., Lee, C., Sultana, C., Ault, A., Axson, J., Martinez, M., Venero, I., Santos-Figueroa, G., Stokes, M., Deane, G., Mayol-Bracero, O., Grassian, V., Bertram, T., Bertram, A., Moffett, B., and Franc, G.: Sea spray aerosol as a unique source of ice nucleating particles, P. Natl. Acad. Sci. USA, 113, 5797–5803, https://doi.org/10.1073/pnas.1514034112, 2016.

Herenz, P., Wex, H., Mangold, A., Laffineur, Q., Gorodetskaya, I. V., Fleming, Z. L., Panagi, M., and Stratmann, F.: CCN measurements at the Princess Elisabeth Antarctica research station during three austral summers, Atmos. Chem. Phys., 19, 275–294, https://doi.org/10.5194/acp-19-275-2019, 2019.

McCluskey, C., Hill, T., Humphries, R., Rauker, A., Moreau, S., Strutton, P., Chambers, S., Williams, A., McRobert, I., Ward, J., Keywood, M., Harnwell, J., Ponsonby, W., Loh, Z., Krummel, P., Protat, A., Keidenweis, S., and DeMott, P.: Observations of ice nucleating particles over Southern Ocean waters, Geophys. Res. Lett., 45, 11–989, https://doi.org/10.1029/2018GL079981, 2018.

Mitts, B. A., Wang, X., Lucero, D. D., Beall, C. M., Deane, G. B., DeMott, P. J., and Prather, K. A.: Importance of Supermicron Ice Nucleating Particles in

Nascent Sea Spray, Geophys. Res. Lett., 48, e2020GL089 633, https://doi.org/10.1029/2020GL089633, 2021.

Radenz, M., Seifert, P., Baars, H., Floutsi, A. A., Yin, Z., and Bühl, J.: Automated time–height-resolved air mass source attribution for profiling remote sensing applications, Atmos. Chem. Phys., 21, 3015–3033, https://doi.org/10.5194/acp-21-3015-2021, 2021.

Sprenger, M. and Wernli, H.: The LAGRANTO Lagrangian analysis tool – version 2.0, Geosci. Model Dev., 8, 2569–2586, https://doi.org/10.5194/gmd-8-2569-2015, 2015.

Thurnherr, I., Wernli, H., and Aemisegger, F.: 10-day backward trajectories from ECMWF analysis data along the ship track of the Antarctic Circumnavigation Expedition in austral summer 2016/2017., Zenodo [data set], https://doi.org/10.5281/zenodo.4031705, 2020.